Journal of CO2 Utilization 78 (2023) 102636

Contents lists available at ScienceDirect

Journal of CO2 Utilization

journal homepage: www.elsevier.com/locate/jcou

One-pot growth of metal-organic frameworks on polymers for catalytic performance enhancement in the CO_2 cycloaddition to epoxides

Julián E. Sánchez-Velandia [a], Ferran Esteve [a,b], Miguel Maireles [a], Diego Iglesias [c], Nuria Martín [a], Marcileia Zanatta [c], Victor Sans [c], Francisco G. Cirujano [a,*], Eduardo García-Verdugo [a,*]

[a] Grupo de Química Sostenible y Supramolecular, Departamento de Química Inorgánica y Orgánica, Universidad Jaume I, Av. Sos Baynat, s/n, Castelló de la Plana, Castellón 12071 Spain
[b] Laboratoire de Chimie Supramoléculaire, Institut de Science et d'Ingénierie Supramoléculaires (ISIS), Université de Strasbourg, Strasbourg 67000, France
[c] Institute of Advanced Materials (INAM), Universitat Jaume I (UJI), Avenida de Vicent Sos Baynat, s/n, Castelló de la Plana, Castellón 12071 Spain

ARTICLE INFO

Keywords:
MOFs
3D-printed polymers
Heterogeneous catalysis
CO2 fixation
Cyclic carbonates

ABSTRACT

A novel approach is reported to prepare 3D-printed polymers that incorporate metal-organic frameworks (MOFs) through a one-pot growth process, involving covalent grafting and growth onto 3D polymeric surfaces. The resulting hybrid materials were subjected to comprehensive characterization using techniques such as SEM, XRD, FTIR, Raman, and XPS. The findings demonstrated an excellent dispersion of the inorganic units on the polymer matrix while preserving their metal-organic structure. The hybrid materials exhibited the presence of Lewis acid and basic groups within the MOF. The catalytic performance of these hybrid materials was evaluated in the mild cycloaddition reaction of carbon dioxide (CO_2) to epoxides. Notably, the polymers incorporating UiO-67 MOFs displayed remarkable activity, even at low CO_2 pressures and in the absence of auxiliary co-catalysts or additives. The catalytic activity of these hybrid materials exhibited a significant improvement, up to two orders of magnitude higher than analogous bulk MOFs. This observation highlights the superior performance of the 3D-printed polymer/MOF hybrids in this catalytic transformation.

1. Introduction

Metal-organic frameworks (MOFs) are crystalline, porous, and tailorable materials with high potential as recyclable heterogeneous catalysts [1–4]. For most of the traditional applications of MOFs, their typical powder form (in the scale from nano- to micrometers) has proved as a straightforward and useful methodology. However, this approach presents some limitations when aiming for high catalytic activity and durability in the production of fine chemicals and pharmaceutically active compounds [5]. On the one hand, only a small part of the active sites participates in the activation of the reaction substrates, especially for large crystals with low surface-to-volume ratios. Besides, MOFs often suffer from deactivation as a direct result of agglomeration and mechanical attrition over consecutive reaction cycles (Scheme 1, left). Many efforts have been devoted in the last decade to enhancing the catalytic activity and stability of MOFs by means of their incorporation into oriented matrixes such as granules and pellets. Nevertheless, this methodology often results in a significant loss of surface area, material deactivation/deformation, and limited access to pores [6–8].

Recent reports show precedents of incorporating MOFs, particularly ZIF-8 and H-KUST-1, onto the surface of standalone (3D-printed) polymers through non-covalent methods [9–14]. Some studies have also attempted covalent grafting of pre-synthesized MOFs onto polymer supports by reacting amino groups of the linker with epoxy groups of the polymer [15–18]. However, these systems have faced challenges such as a significant decrease in activity attributed to crystal agglomeration during the post-synthetic grafting step and the potential leaching of metal species from the MOFs (refer to Scheme 1, center). Although these approaches show promise, these issues have limited their effectiveness in practical applications [2,3,6,8].

Additive manufacturing (AM), commonly known as 3D printing (3DP), offers unique advantages in generating complex and customized geometries that are often difficult or expensive to achieve through traditional manufacturing methods. This technology enables the

* Corresponding authors.
E-mail addresses: cirujano@uji.es (F.G. Cirujano), cepeda@uji.es (E. García-Verdugo).

https://doi.org/10.1016/j.jcou.2023.102636
Received 27 September 2023; Received in revised form 27 November 2023; Accepted 29 November 2023
Available online 5 December 2023

creation of scaffolds with intricate structures, which can be seamlessly integrated into complex 3D architectures. In our study, we have developed an innovative approach for the in-situ growth of zirconium carboxylate metal-organic frameworks (MOFs) on 3D-printed epoxy-functionalized polymeric surfaces (refer to Scheme 1, right). The presence of epoxy functional groups on the surface enables precise surface customization by introducing aromatic carboxylate moieties through the ring-opening of these epoxy groups with amino-functionalized linkers, such as 2-amino terephthalic acid or 3-aminobenzoic acid (see Fig. 1). The precise incorporation of carboxylate groups onto the polymeric surface facilitates the grafting of metal species and subsequent nucleation and growth of the MOF crystals on the surface of the 3D polymeric network.

This approach allows us to capitalize on the inherent advantages of MOFs, including their potential catalytic properties and remarkable CO_2 adsorption capabilities, while leveraging 3D printing technologies to fabricate intricate polymeric frameworks for the activation and conversion of CO_2, particularly in the context of the cycloaddition of CO_2 to epoxides. Notably, the polymers incorporating UiO-67 MOFs exhibited exceptional catalytic activity, demonstrating remarkable performance even at low CO_2 pressures and without the need for auxiliary co-catalysts or additives. In fact, the catalytic activity of these hybrid materials showed a significant enhancement, reaching up to two orders of magnitude higher than that of comparable bulk MOFs.

2. Results and discussion

2.1. 3D printed polymer surface modification and MOF growth and immobilization

The 3D printed polymeric supports were obtained from the photopolymerization of glycidyl methacrylate (GMA) and additional acrylate-based crosslinkers either ethylene glycol methacrylate (EGMA) or 1,4-butanediol diacrylate (1,4-BUDA) in the presence of phenylbis (2,4,6-trimethylbenzoyl)-phosphine oxide (BAPO) as the photo-initiator, as shown in the step (i) of Fig. 1 [19]. Proof-of-concept macroscopic structures, in the form of 3DP devices resembling simple disks (10 mm diameter, 1.5 mm high), were utilized to explore the feasibility of in-situ MOF growth. The choice of these devices was motivated by their relatively uniform and flat surfaces, facilitating subsequent characterization efforts. Initially, the focus was on immobilizing UiO-66-NH_2 on the polymer surface. The amino groups present in the 2-aminoterephthalic acid linkers could serve as nucleophiles, enabling the ring-opening of the epoxy groups on the polymer support (step ii in Fig. 1). This reaction results in the formation of covalent bonds between the MOF linkers and the polymer. Therefore, it enables the in-situ growth of MOFs within the structure (step iii in Fig. 1) and their direct immobilization onto the polymer surface in a one-pot methodology (Material 1 A in Fig. 1).

It is worth mentioning that the immobilization and growth of the MOF on the polymer surface can also be achieved using a one-pot methodology. In this approach, the modification of the polymer surface occurs concurrently with the growth of the MOF (step iv in Fig. 1). This one-pot method offers the advantage of simplifying the process by combining the surface modification and MOF growth steps into a single reaction, facilitating the integration of the MOF onto the polymer surface in a more efficient and streamlined manner (Material 1 A in Fig. 1).

Thus, in a preliminary experiment, the disc was subjected to modification using solely 2-aminoterephthalic acid (BDC-NH_2) to confirm the successful grafting of the linker onto the polymer surface. The success of this modification was verified through ATR-FT-IR analysis of the disc (Fig. 2). The resulting spectrum displayed significant changes, including an increase in intensity for the O-H band at approximately 3500 cm^{-1}, the presence of a carbonyl band within the range of 1600–1700 cm^{-1}, and the C-N amine stretching band at around 1350 cm^{-1}. Additionally, the modification of the C-H and C-O stretching bands in the 750–1100 cm^{-1} region indicated the effective modification of the epoxy groups present in the polymer. Noteworthy, the appearance, after the disc modification with 2-aminoterephthalic acid (BDC-NH_2-A in Fig. 2), of a new peak at 1680 cm^{-1} corresponding to C═O of free carboxylic acid groups indicates the incorporation of free carboxylic acid groups onto the polymer surface readily available for the subsequent MOF growth [20].

After the surface modification process is finalized, the 3D-printed polymer is ready for MOF growth. The growth of MOF crystals takes place through a self-assembly process, driven by coordination interactions between the metal ions and the organic linkers under solvothermal conditions and in the presence of the modified polymeric disc using an excess of 2-aminoterephthalic acid and $ZrCl_4$, following the detailed procedure outlined in the experimental setup. It's worth emphasizing that the MOF organic precursor can directly induce the epoxide ring-opening reaction of the precursors. Consequently, MOF growth can also be performed directly on the non-modified polymer surface in a "one-pot, one-step" fashion, without the necessity of pre-anchoring the MOF linker (step iv of Fig. 1) yielding analogous results. Following the growth process and subsequent washing, the modified polymers exhibited the presence of MOF crystallites on the

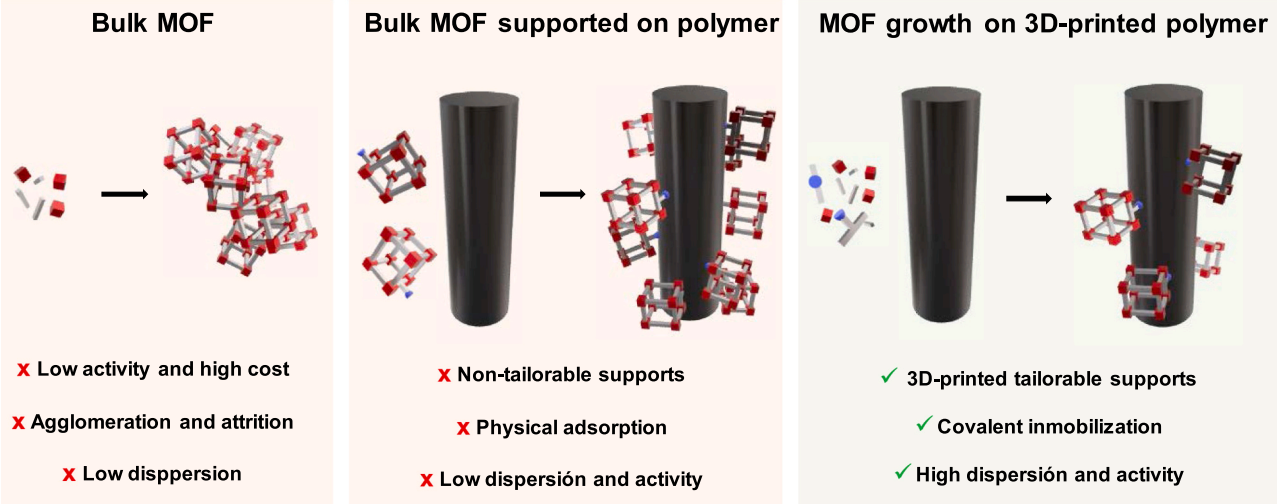

Scheme 1. Representation of state-of-art MOF technologies based on bulk powder (left) and post-synthetic adsorption of MOFs on polymer surfaces (center); in comparison with the approach proposed in this work based on the one-pot growth of MOF on 3D-printed materials with functional groups for the covalent immobilization of the MOF (right).

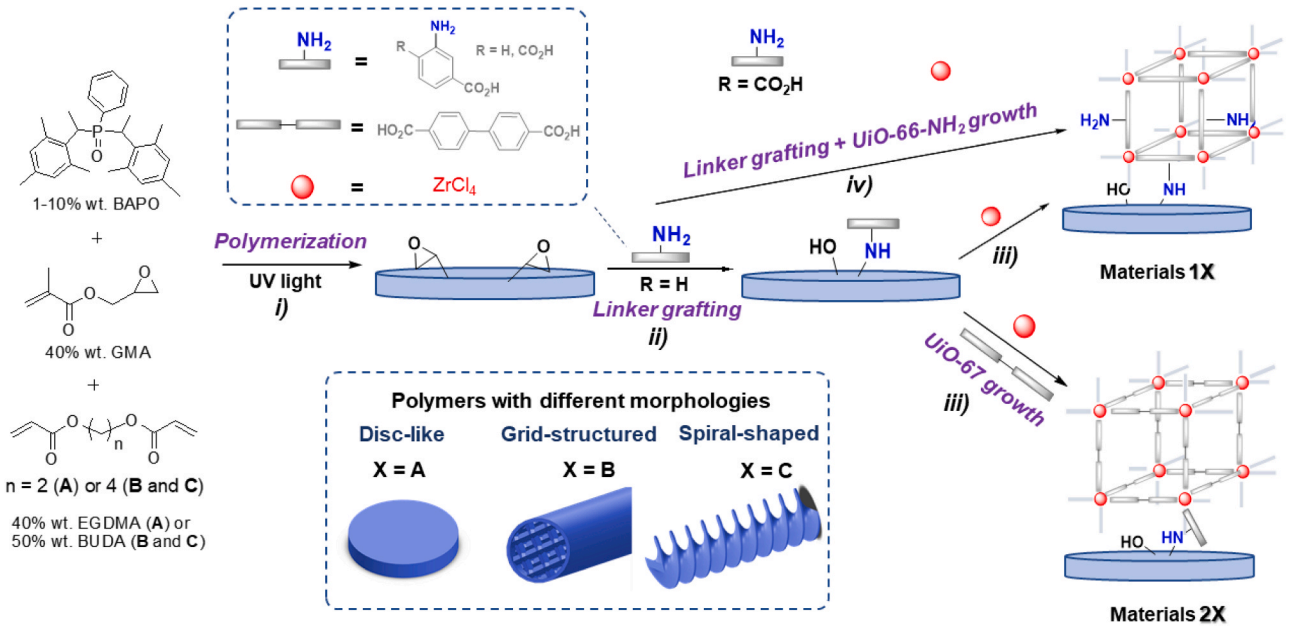

Fig. 1. Schematic representation of the synthetic protocol for different MOF-3DP-polymers composites. 1X refers to materials bearing UiO-66-NH_2 as supported MOF and 2X based on UiO-67. X refers to the 3D structure of the polymer scaffold studied in this work: disc-like (1 A and 2 A); grid-structured (1B and 2B); and spiral-shaped (2 C). See ESI for synthetic details.

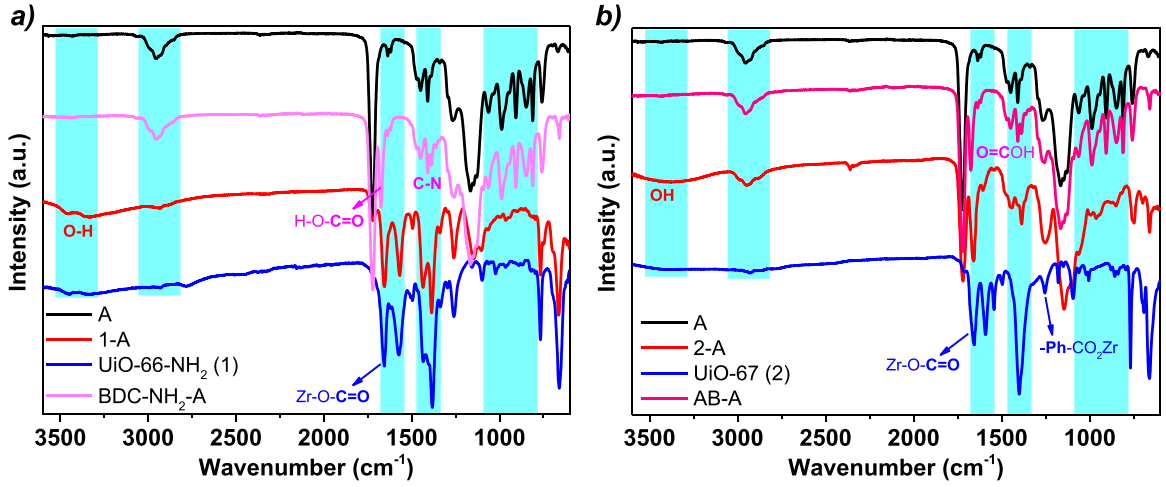

Fig. 2. FTIR of the polymer disc A (black spectrum), disc grafted with BDC-NH_2 = 2-amino terephthalic acid (a) or AB= 3-aminobenzoic acid (pink spectrum) and subsequent in-situ growth of UiO-66-NH_2 (a) or UiO-67 MOF on the disc (1 A and 2 A) (red spectrum) and bulk UiO-66-NH_2 (a) or UiO-67 MOF (b) (blue spectrum). The most characteristic bands discussed in the text have been highlighted in light blue and associated to the characteristic functional groups of the MOF.

surface. This was confirmed through characterization by different techniques. The ATR-FT-IR spectrum of material 1 A displayed characteristic bands of the bulk UiO-66-NH_2 MOF (as shown in the red and blue spectra in Fig. 2), like the carbonyl band of zirconium carboxylate bonds at 1650 cm^{-1}.

Besides, the evaluation of UiO-66-NH_2 crystals on the polymer surface using scanning electron microscopy (SEM), Raman spectroscopy, X-ray diffraction (XRD) and X-ray photoelectron spectroscopy (XPS) provided additional evidence of the immobilization of the MOFs. Thus, the SEM images, as shown in Fig. 3a, validate the uniform decoration of the polymeric surface with MOF, observed at both the micro- and nanoscale. The SEM images reveal the presence of MOF crystallites with diameters ranging from approximately 100 to 500 nm, confirming the successful formation and distribution of MOF structures on the polymeric surface (Fig. 3a).

To demonstrate the versatility of this methodology for the in-situ growth and immobilization of other MOFs, UiO-67 was chosen as an additional example. Unlike UiO-66-NH_2, UiO-67 does not contain amino groups in its structure. Therefore, the immobilization and growth of UiO-67 on the polymer surface can only occur after the surface modification of the 3D-printed polymers is completed. For the surface modification step, 3-aminobenzoic acid was selected as the molecule to modify the surface and facilitate the growth and immobilization of UiO-67. The 3-aminobenzoic acid molecules react with the epoxide moieties of the polymer to modify the surface, allowing for the subsequent growth and attachment of UiO-67 crystals on the polymer surface. This "one-pot two-step" modification provides the necessary functional groups for coordination with the metal ions of UiO-67 and enables the successful immobilization of the MOF on the polymer surface (see step (iii) in the bottom part of Fig. 1), as indicated by the carbonyl vibration band at 1675 cm^{-1} assigned to the free carboxylic acid groups of the 3-aminobenzoic acid grafted to the polymer (see Fig. 2).

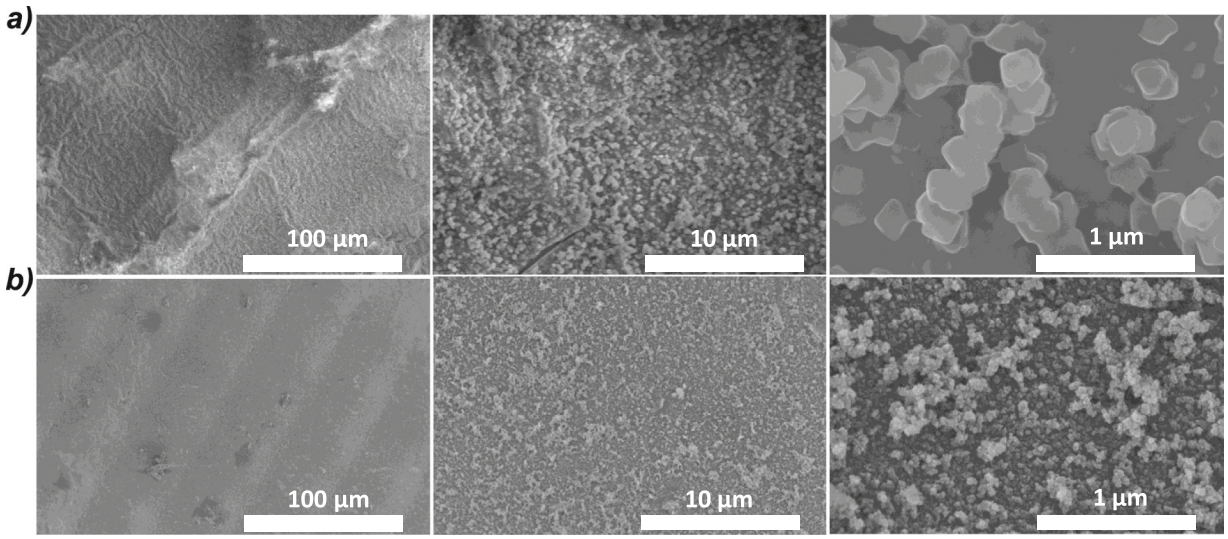

Fig. 3. SEM images of the 3D printed polymeric disc modified with MOF samples 1 A (a) and 2 A (b). A gradual increase in augments can be observed from left to right, shifting from microscopic (left, 100 µm) to nanoscopic scale (left, 1 µm).

Following the successful modification of the polymer with 3-aminobenzoic acid, as confirmed by ATR-FT-IR analysis (refer to Fig. 2), the solvothermal growth of UiO-67 MOF was carried out using 1,1′-biphenyl-4,4′-dicarboxylic acid and $ZrCl_4$ (as shown in Fig. 1). The ATR-FT-IR analysis of the hybrid material obtained demonstrates the presence of characteristic peaks associated with UiO-67, such as 1660 cm^{-1} assigned to C═O groups of the zirconium carboxylates and 1260 cm^{-1} corresponding to aromatic moieties from the 1,1′-biphenyl-4,4′-dicarboxylic acid linker (Fig. 2b). These spectral features confirm the successful incorporation of UiO-67 onto the modified polymer surface. Furthermore, the SEM images provide evidence of the homogeneous distribution of UiO-67 nanoparticles throughout the surface of the disc (Fig. 3b). The images confirm the successful growth of the MOF on the modified polymer and reveal the formation of uniformly dispersed UiO-67 nanoparticles, with sizes smaller than 50 nm.

These experimental findings provide compelling evidence of the effectiveness of the growth methodology in achieving the desired growth and dispersion of UiO-67 on the polymer surface. The SEM images indicate that UiO-67 exhibits a smaller particle size compared to UiO66-NH_2. The nucleation and crystal growth of the $Zr_6O_4(OH)_4$ secondary building unit (SBU) in UiO-67 are known to be challenging and highly sensitive to reaction conditions for this two aromatic ring system (4,4′-biphenyl dicarboxylate) with respect to the above mentioned one aromatic ring (1,4-benzene dicarboxylate) UiO-66 system. This has been attributed to the distorting of the Zr–O bonds between the $Zr_6O_4(OH)_4$ SBU and the organic linker with two aromatic rings due to the torsion of the biphenyl, which does not exist in the case of the one-ring benzene dicarboxylate [21]. Such torsional strain that is experienced in the crystalline structure, results in a more probable UiO-67 structural breakdown with respect to the "torsional strain-free" UiO-66 structure.

Therefore, precise control is necessary to maintain suitable conditions throughout synthesis and handling to ensure the integrity and optimal performance of the MOF. Acetic acid has been utilized as a modulator to regulate the nucleation and crystal growth of UiO-67, playing a critical role in controlling the size, morphology, and uniformity of the resulting crystals. However, it is important to note that attempting to grow UiO-67 under strong acid conditions has detrimental effects on the structure of the 3D-printed polymer. This deterioration can be attributed to the hydrolysis of ester groups present in the monomers used for polymer preparation. To mitigate such adverse effects, careful consideration must be given to the compatibility between the reaction conditions and the polymer matrix in MOF growth experiments.

Raman mapping is a versatile and powerful technique for characterizing material surfaces, providing valuable insights into their chemical composition, molecular structure, surface topography, and spatial distribution. In the case of 3D-printed MOF hybrids, Raman mapping was utilized to investigate the chemical composition and molecular structure of the MOF and visualize their surface topography and MOF thicknesses. This comprehensive characterization approach helps uncover the surface properties and behavior of the MOF-polymer hybrid system, shedding light on the distribution and arrangement of the MOF within the polymer matrix.

Through the combination of chemical information and visual mapping, Raman mapping allows for a deeper understanding of the distribution of the MOF at the surface of the hybrid material [22]. The Raman depth mapping analyses of the hybrids reveal two distinct components (Fig. 4). The first component, represented by the red color for both samples 1 A and 2 A (as seen in the top part of Fig. 4a and b), exhibits the main Raman shifts characteristic of either bulk UiO-66-NH_2 (as shown in Fig. 4a and the middle spectra of part c) or bulk UiO-67 (as depicted in Fig. 4b and the top spectra of part c). This component corresponds to the Raman signals originating from the MOF crystals present on the surface and matches with the main signals of the bulk MOFs. Several Raman signals corresponding to the MOF linker can be identified in this component for both MOF/polymer composites: 850 cm^{-1} (1 A) or 855 cm^{-1} (2 A) for the C-C symmetric breathing mode; 1120 cm^{-1} (1 A) or 1155 cm^{-1} (2 A) for the antisymmetric C-H wagging of benzene/aromatic ring breathing mode; 1440 cm^{-1} (1 A) or 1445 cm^{-1} (2 A) for the O-C-O symmetric stretching and 1615 cm^{-1} (1 A) or 1610 cm^{-1} (2 A) for the C-C symmetric ring breathing mode of the linker [23].

The second component in depth, represented by the blue color for both samples 1 A and 2 A (as observed in the bottom part of Fig. 4a and b), can be identified as the polymer component. This identification is based on the Raman shifts characteristic of the acrylate groups present in the bulk polymeric material. For example, the signal at 1720 cm^{-1}, assignable to the ester groups of the polyacrylate, confirms the presence of the polymer component (as illustrated in Fig. 4c, bottom spectra). This analysis reveals notable disparities in the distribution of the MOF (represented by the red component in Fig. 4) across the surfaces of samples 1 A and 2 A. Sample 1 A, decorated with UiO-66-NH_2, demonstrates a denser distribution of the MOF phase (Fig. 4a), whereas sample 2 A, decorated with UiO-67, displays a thinner (<10 µm) and slightly more dispersed distribution of the MOF phase (Fig. 4b). This might be a result of the poor crystallization of UiO-67 with respect to the UiO-66-NH_2, as suggested by SEM and will be confirmed by other techniques (XRD, XPS and FTIR) vide infra.

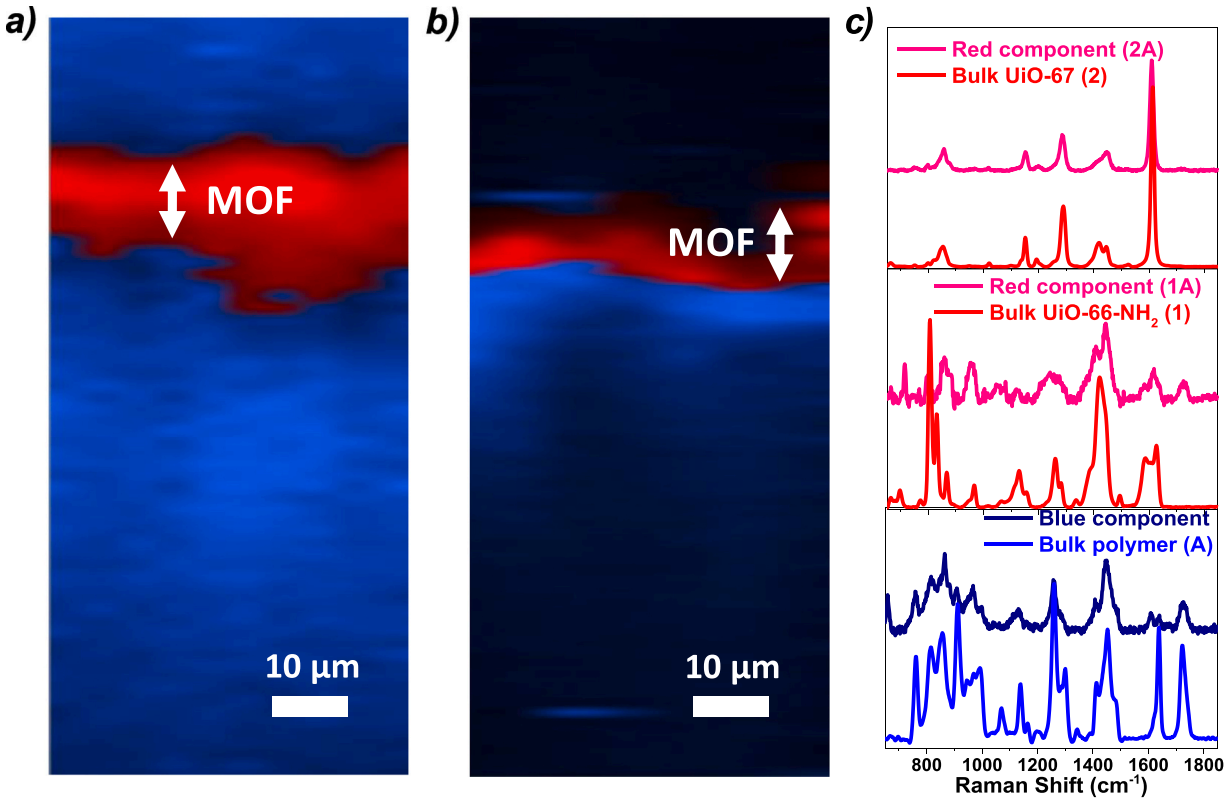

Fig. 4. Raman depth mapping analyses of 1 A (a) and 2 A (b). Regions marked in red correspond to the spatial sections that presented a Raman signal at 1615 cm^{-1} and 1430–1450 cm^{-1} associated with the C-C stretching mode of the aromatic ring and in-phase carboxylate stretching of the linker, respectively (c). The arrows indicating the MOF layer have the same size as the scale at the right bottom part (10 µm).

X-ray diffraction (XRD) is a commonly used technique for the characterization of metal-organic frameworks (MOFs). However, when it comes to hybrid materials incorporating amorphous polymeric supports, the application of XRD can be challenging. The inherent amorphous nature of the polymeric support lacks long-range order, resulting in broad background scattering in the XRD pattern (see broad peak between 10 and 35 ° in Fig. 5 due to polymer disc A). This background scattering can overlap with the diffraction peaks from the MOF, making it difficult to accurately interpret and analyze the XRD data, especially for quantitative measurements of MOF crystallinity. In the case of the in-situ grown UiO-66-NH_2 (sample 1 A), the crystalline structure was confirmed by powder XRD analysis. Two characteristic intense peaks below $2\theta = 10°$, observed in the bulk UiO-66-NH_2 sample, were also present in sample 1 A, providing evidence of the successful incorporation and growth of UiO-66-NH_2 on the polymeric support (refer to 1 A in Fig. 5a). In the case of sample 2 A, the UiO-67 nanoparticles exhibited a smaller size, higher structural strain, and higher dispersion, which is likely to lead to a pronounced broadening of the characteristic XRD peaks observed in the bulk UiO-67 sample (refer to 2 A Fig. 5b). The broadening of these peaks, combined with the amorphous nature of the polymeric support (A), poses challenges in the effective characterization of the MOF by powder XRD. These findings stress the difficulties inherent in studying hybrid materials not in (polycrystalline) powder form (see well-defined patterns of bulk UiO-66 -NH_2 and UiO-67 in

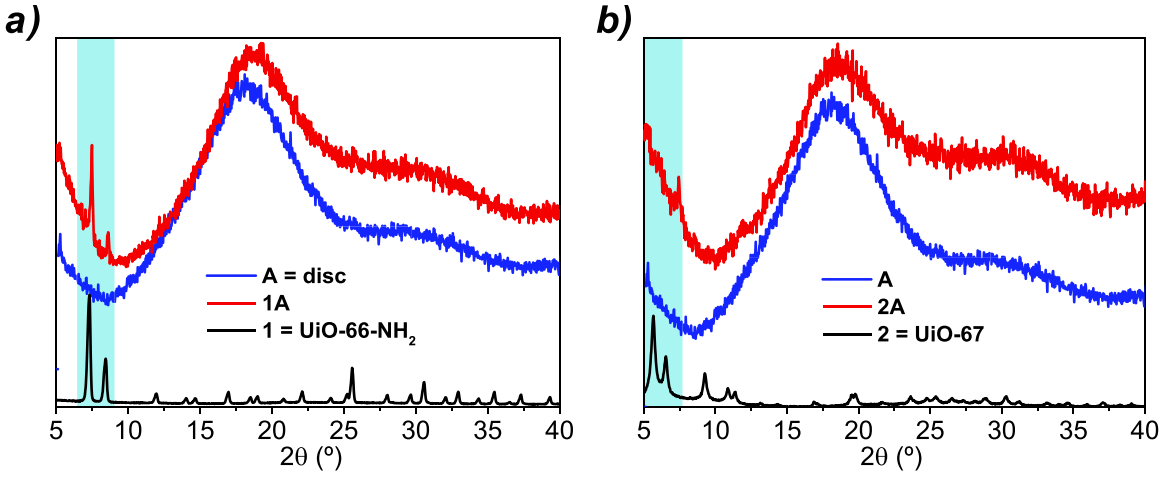

Fig. 5. Powder XRD analyses for samples 1 A (a) and 2 A (b). The amorphous pattern measured for the unmodified polymer disc A has been added (blue pattern). The patterns for the bulk MOFs 1 and 2 have also been introduced in black: UiO-66-NH_2 (a) and UiO-67 (b).

Fig. 5) but grown on a surface and highlight the importance of meticulous interpretation and analysis of XRD data when studying MOF-polymer hybrid systems.

Being the MOF located mainly on the surface, XPS analysis is a more adequate technique with respect to XRD. This technique provided valuable insights into the surface composition and Zr-oxo chemical environments of the UiO-66-NH_2/disc hybrid (sample 1 A). Consistent with expectations, similar signals to those of bulk UiO66-NH_2 were observed on the surface of the MOF-3D-printed disc. The Zr $3d_{3/2}$ (185.2 eV) and Zr $3d_{5/2}$ (182.9 eV) signals indicated the presence of Zr^{4+} in the expected oxidation state and coordination environment. Additionally, signals at 534, 532, and 530 eV were assigned to free carboxylate groups (COOH), metal-coordinated carboxylate groups (Zr-O-C), and bridging linked η_3-O-Zr groups (Zr-O-Zr), respectively. These findings were in accordance with the chemical environment of UiO66-NH_2 (Fig. 6 and Fig. S1).

For UiO-67 (sample 2 A), the high-resolution XPS spectrum of the O1s region displayed a peak at 530.4 eV, which was assigned to Zr-O-Zr bonding units within the MOF structure (Fig. 6b) [24]. Interestingly, more pronounced peaks at > 533 eV were observed in the spectrum of sample 2 A compared to that of sample 1 A. This suggested the presence of uncoordinated carboxylate groups (-COOH) as well as Zr-O-H groups resulting from missing linkers between neighboring Zr_6-oxo clusters, indicating network defects. This observation correlated with a large amount of coordinated-free carboxylate groups (1680 cm^{-1}) present in the FTIR (see Fig. 3), as well as the smaller and less-perfect crystals observed in sample 2 A [24,25]. Moreover, the differences in the Zr 3d signals with respect to the 1 A sample (see additional signals at binding energies >187 eV in Fig. S1) might be related to a different type of Zr coordination environment (i.e. Zr nodes with exposed OH sites or coordinatively unsaturated Zr-O-H sites vs. saturated Zr-O-Zr sites) in the highly defective 2 A sample with respect to sample 1 A, which is in line with the O1s XPS spectrum described above [25].

Overall, understanding and addressing the challenges associated with MOF growth and considering the compatibility of reaction conditions with the polymer matrix is crucial for successful MOF synthesis and maintaining the integrity of the polymer material. After considering and addressing such issues, it is possible to expand the range of MOFs that can be grown and immobilized on the surface of 3D-printed polymers, showcasing the versatility and applicability of this methodology for various MOF systems. The observations made through the surface-sensitive RAMAN, SEM and XPS analyses are consistent, providing further confirmation of the differences in MOF distribution on the polymer surface. The combination of these characterization techniques allows for a comprehensive understanding of the MOF-polymer hybrid system, offering insights into the spatial distribution and heterogeneity of the MOF phase obtained by the methodology here developed.

2.2. 3D printed MOF with more complex 3D structures

Having successfully developed a methodology for the solvothermal growth and immobilization of MOF on the polymeric surface of simple 3D structures like disks, we expanded our approach to more intricate polymer scaffolds. In this study, we evaluated two different 3D structures: grid structures and spiral shape devices, denoted as B and C in Fig. 1c, respectively. To fabricate these polymer scaffolds, we employed a direct polymerization approach using a mixture of glycidyl methacrylate (GMA) and 1,4-butanediol diacrylate (1,4-BUDA) with a weight ratio of 50:50%. Phenylbis(2,4,6-trimethylbenzoyl)-phosphine oxide (BAPO) was included as the photoinitiator (see Fig. 1) in a 1% wt. The incorporation of 1,4-butanediol diacrylate (1,4-BUDA) into the polymer formulation enabled the production of 3D structures with enhanced spatial definition and complexity.

The developed methodology was applied to modify the surfaces of polymers B and C, printed with different 3D geometries. 2-aminoterephthalic acid was used to open the epoxide groups on the polymers,

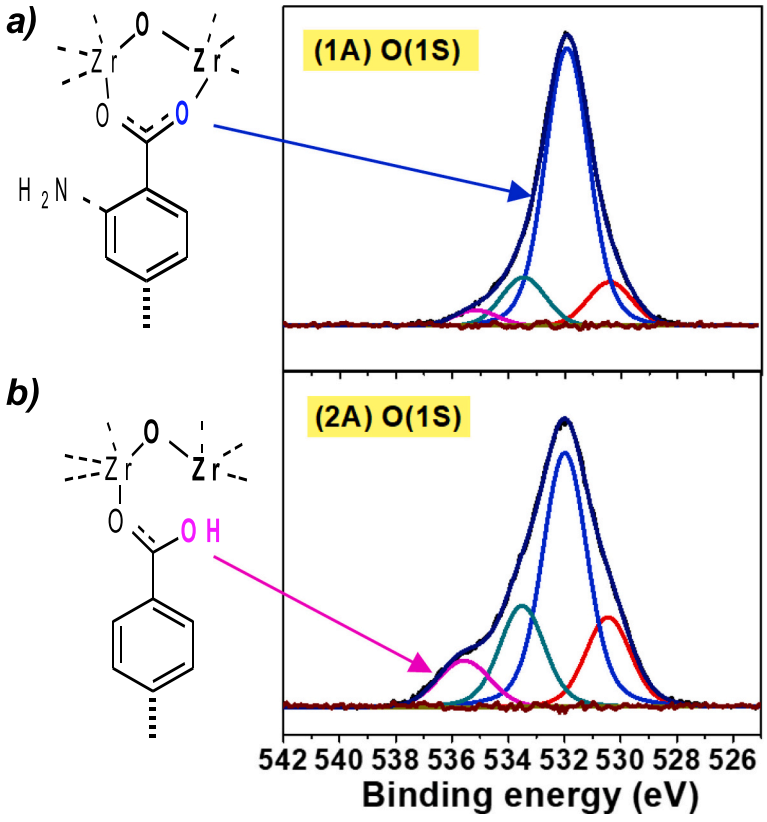

Fig. 6. O(1 S) XPS analysis of 1 A (a) and 2 A (b). The chemical structures of the proposed motifs present in the crystals have been included in the left part. See Figure. S1 for comparison with the spectra of the 1 bulk MOF.

thereby facilitating the grafting of the MOF. The success of this modification was confirmed by observing the disappearance of C-O oxirane vibrations at approximately 750–1100 cm^{-1} and the appearance of O-H bonds at around 3500 cm^{-1} (Fig. S2). Subsequently, the solvothermal synthesis of the MOF was performed, and upon analyzing the resulting samples by ATR-FT-IR, we found clear evidence of the MOF's growth on both polymer surfaces, regardless of their geometries, by the presence of a zirconium carboxylate vibration band characteristic of metal-carboxylate interactions, as well as metal-oxo vibrations at approximately 1600–1700 cm^{-1} and 700–800 cm^{-1}, for both UiO-66-NH_2 (1 C) and UiO-67 (2 C) MOFs (Fig. S2). As previously mentioned, the low MOF loading, together with the amorphous nature and the high curvature of the polymeric supports does not provide a substantial diffraction pattern of the grafted MOF crystalline structure (Fig. S3).

The ICP analysis results of the acid hydrolysis MOF/polymer samples provided valuable insights into the Zr content of the hybrid materials that were prepared. The analysis showed that the Zr content varied across the different samples, but overall, the Zr loading was relatively low, ranging from 0.6 to 1.9 mg Zr per gram of MOF-3D-printed polymer (see Table S1). These findings are consistent with the expectation of simple surface attachments of the MOF onto the polymer surface as observed for the simpler disc geometry. The SEM images of sample 2 C (Fig. S5a) clearly show the uniform presence of the MOF UiO-67 on the surface of the polymer. However, the size of the MOF particles on this sample appears slightly larger compared to those obtained by growing the MOF on the polymer with a disc geometry. This difference in morphology is likely to be related to the influence of the support geometry on the growth of the MOF. Different geometries of the polymer support can affect the nucleation and growth processes of the MOF crystals [26]. The surface area, surface energy, and physical structure of the polymer could play significant roles in guiding the nucleation and subsequent crystal growth of the MOF. Indeed, Fig. S5 shows the presence of the denser MOF growth in the edge of the spiral geometry (see image in the center of Fig. S5b), even after 3 consecutive reaction cycles.

2.3. Catalytic evaluation of the 3D-printed-MOF hybrid

MOFs can be used across a broad spectrum of applications, spanning gas storage, sensing, catalytic processes, etc [2–5]. To assess the applicability of hybrid materials obtained by growing MOFs on 3D-printing polymeric scaffolds, we decided to evaluate their viability for catalyzing the activation and conversion of CO_2. MOFs not only exhibit the capacity to adsorb CO_2 but also possess functional groups that serve as active sites for CO_2 activation. These groups include Lewis acids, basic functional moieties, and nucleophilic sites, which emerge due to network imperfections. We chose the cycloaddition reaction between CO_2 and epichlorohydrin as our benchmark reaction, given its well-documented nature [27–29]. The catalytic transformation was assayed at 80 °C in the presence of a CO_2 balloon for 5 h. Kinetic profiles were monitored by withdrawing samples from the catalytic crude every 30 min during the reaction time (5 h). The conversion, selectivity and yield of the epoxide into the desired cyclic carbonate were calculated by the combined use of FTIR and NMR spectroscopy (Figs. S4 and S6 and Tables S1 and S2),

In the absence of a co-catalyst, $ZrCl_4$, the modified polymeric scaffolds, and the bulk MOF did not exhibit significant catalytic activity (Entries 1–5, Table S1). Only UiO-66-NH_2 showed a minor conversion (Fig. 7 Table S1). As for the hybrid MOF-3D printed polymer composites, those containing UiO-67 components demonstrated superior catalytic performance compared to their UiO66-NH_2 counterparts (Fig. 7, Table S1). In all the cases, the reaction proceeded with remarkable selectivity (> 99%) in each instance, yielding only the respective carbonate product. Indeed, the top-performing materials were as follows: 2B (yielding 61%) > 2 C (yielding 50%) > 2 A (yielding 10%) > UiO-67 bulk (yielding <2%). It's important to emphasize that these outcomes are quite promising, particularly considering that the CO_2 conversion

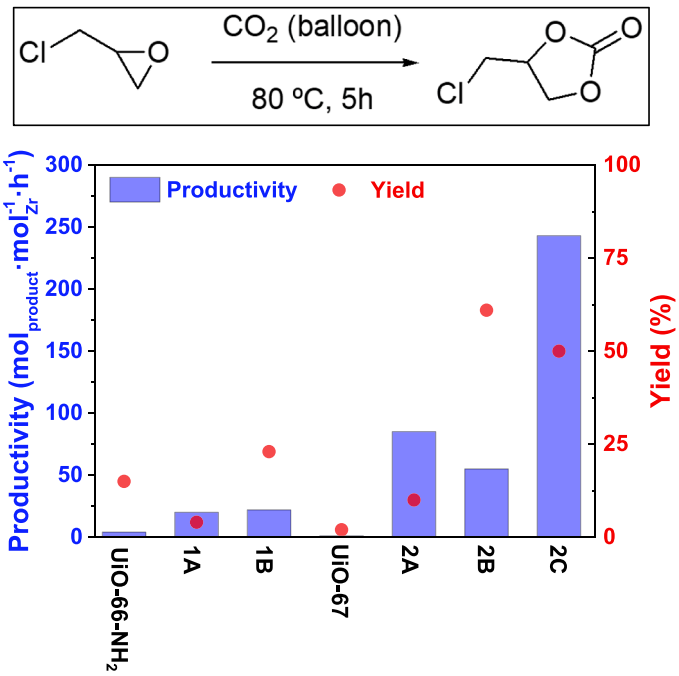

Fig. 7. Productivity (left axis, expressed in mols of carbonate product obtained divided by the moles of Zr and by the reaction time) and yield after 5 h of reaction (right axis) obtained with MOFs 1 (UiO-66-NH_2) and 2 (UiO-67) either in bulk or grown on polymers A, B and C, during the CO_2 cycloaddition to epichlorohydrin. Reaction conditions: 0.5 mL epichlorohydrin, 80 °C, CO_2 balloon, solvent/additive-free.

reaction was conducted without the assistance of supplementary co-catalysts [30].

For the hybrid MOF-3D printed polymer grown on disc-like materials (1 A and 2 A), the catalytic activity seems to correlate with the number of defects (which causes more unsaturated metal sites that can active the epoxides) as well as particle size, following the anticipated inverse trend. The enhanced productivities observed in 2 A compared to 1 A stem from the greater presence of structural defects (i.e. missing linkers) evident in the former UiO-67-derived material, as indicated by XPS analyses (Fig. 6). The higher number of defects in UiO-67 causes more unsaturated metal sites that can activate the epoxides. Moreover, smaller and more defective MOF nanoparticles lead to higher yields of cyclic carbonate, as depicted in Fig. 7. Specifically, materials 1 A (with particle size >200 nm) yielded productivities of 20 $mol_{product}·mol_{Zr}^{-1}$ h^{-1}, whereas 2 A (with particle size <50 nm) achieved significantly higher productivity at 85 $mol_{product}·mol_{Zr}^{-1}$ h^{-1}. Additionally, the higher porosity inherent in UiO-67 likely contributes to the improved catalytic performance of 2 A [2,3,21–23].

When considering the impact of the 3D morphology of the polymeric scaffolds, the highest yield was achieved when utilizing 2B, which features a grid-like structure. This enhanced yield associated with 2B was attributed to its higher Zr content in comparison to both 2 A and 2 C. However, it's noteworthy that 2 C exhibited the highest productivity value (243 $mol_{product}·mol_{Zr}^{-1}$ h^{-1}), a nearly five-fold increase compared to 2B (55 $mol_{product}·mol_{Zr}^{-1}$ h^{-1}) and a three-fold increase compared to 2 A (85 $mol_{product}·mol_{Zr}^{-1}$ h^{-1}). Thus, comparing these results to those obtained from bulk UiO-67 (<1 $mol_{product}·mol_{Zr}^{-1}$ h^{-1}), a substantial increase of up to two orders of magnitude was observed for the MOF grown on these 3D-printed polymers (refer to Fig. 7 and Table S1). Consequently, even samples with very low Zr-MOF loading showcased enhanced catalytic performance, likely attributed to improved dispersion and minimal self-deactivation through nanoparticle aggregation.

Furthermore, it's worth highlighting that the composite material 2 C features a distinctive spiral-like structure, which not only contributes to

superior catalytic performance but also maintains a more durable morphology when compared to 2 A and 2B. These latter materials, upon modification with the MOF, exhibit a certain degree of fragility that results in some degradation of the material's structure during the catalytic transformation, as depicted in Fig. S4b. The growth of the MOF on the disc-shaped (A) and grid-structured (B) polymers evidently introduced fragility to the surface, whereas the spiral-shaped material (2 C) displayed greater robustness. This enhanced resilience of 2 C can be attributed to its unique design, which facilitates the even distribution of structural tensions. Besides, the curved surface of 2 C could potentially aid the diffusion of reagents throughout the polymeric matrix, leading to an increase in their local concentration and thereby promoting their reaction. This phenomenon likely accounts for the notable high yields achieved by 2 C (approximately 50%), despite the relatively low catalytic loading of Zr present.

In order to take advantage of the heterogeneous nature of the polymeric matrixes used, the reusability of the material **2 C** was assayed. The recyclability test relied on filtration-based mixture removal of the epichlorohydrin after partial consumption (ca. 70%). Afterwards, a new batch of reagent (0.5 mL of epichlorohydrin) was immediately put in contact with the reactor and the reaction course was monitored until the desired yield was reached.

Results in Fig. 8 and Table S2 indicate that the sample could be successfully reused for at least three reaction cycles, maintaining its catalytic activity (TOF of ca. 130–140 h^{-1} and TON = 1600–1700). This outcome, suggests that (despite the strong curvature of the polymer support) most of the UiO-67 nanocrystals had been covalently grafted on the polymeric surface **C**, preventing the material from experiencing leaching during consecutive reaction cycles. The higher amount of cyclic carbonate detected at initial reaction times in the second and third runs (with higher TOFs of ca.140 vs. 130) was assigned to the adsorption of some products within the hybrid material during the mixture removal, as the polymers were not washed before consecutive runs. To analyze whether any significant morphological change occurred on the polymeric surface during the consecutive catalytic experiments, the reused material was characterized by SEM (Fig. S5). The morphology, size, and distribution of the MOF **2** nanoparticles grafted on polymer **C** were preserved after 3 reaction cycles. Moreover, the Zr content (obtained from ICP analysis of the digested sample) of the spent materials (0.79 $mg_{Zr}{\cdot}g^{-1}_{catalyst}$), was similar to the as-prepared sample (0.83 $mg_{Zr}{\cdot}g^{-1}_{catalyst}$), confirming the stability of the MOF-polymer composite under reaction conditions. Additional recycles showcase a similar cyclic carbonate yield (ca. 70% after 5 h), indicating the adequate MOF grafting, further contributing to the overall mechanical stability and therefore reusability.

The outstanding robustness of **2 C** encouraged us to test the performance of this material under continuous-flow conditions [19]. Preliminary results reveal a stable catalytic activity over a period of 24 h with a productivity of 5.2 $mol_{product}{\cdot}mol^{-1}_{Zr}{\cdot}h^{-1}$ (Fig. S6). More detailed studies assaying the flow usage of such MOF/polymers are ongoing to further increase the applicability and sustainability of the whole process.

The insights already gained from the characterization of the analogous bulk UiO-MOF contribute significantly to the understanding of the acid-base properties, providing essential context for our current study on CO_2 utilization [31]. On the one hand, NH_3-TPD analysis as a Brønsted base probe demonstrated that bulk UiO samples predominantly interact with Brønsted acid sites (Zr–H_2O/Zr–OH) and hard Lewis acid sites on Zr^{4+} with open coordination formed by the missing linkers and dependent on the sample water content. On the other hand, in-situ FTIR of CO performed for the bulk UiO samples revealed the presence of coordinatively unsaturated (cus) Zr^{4+} ions acting as Lewis acid sites [32]. The reported results indicated an expected increase in the amount of Zr Lewis acid sites and Brønsted acid sites associated with water molecules, with the concomitant amount of missing linker defects in UiO samples. This comprehensive analysis underscores the multifaceted nature of the acid-base properties in defect-containing UiO-type MOFs, shedding light on both Lewis and Brønsted acid sites. In this work, we have found that sample 2 A exhibits a higher amount of defects than sample 1 A (as indicated by XPS analysis), and based on the above-mentioned results, material 2 (UiO-67) will present a higher number of Lewis/Brønsted acid sites (associated to such defect-sites) than material 1 (UiO-66-NH_2) when grown on a similar polymer support.

In light of these findings, further studies were performed with the **C** polymer to shed light on the role played by each component of **2 C** in the catalytic transformation. When **C** was only functionalized with the

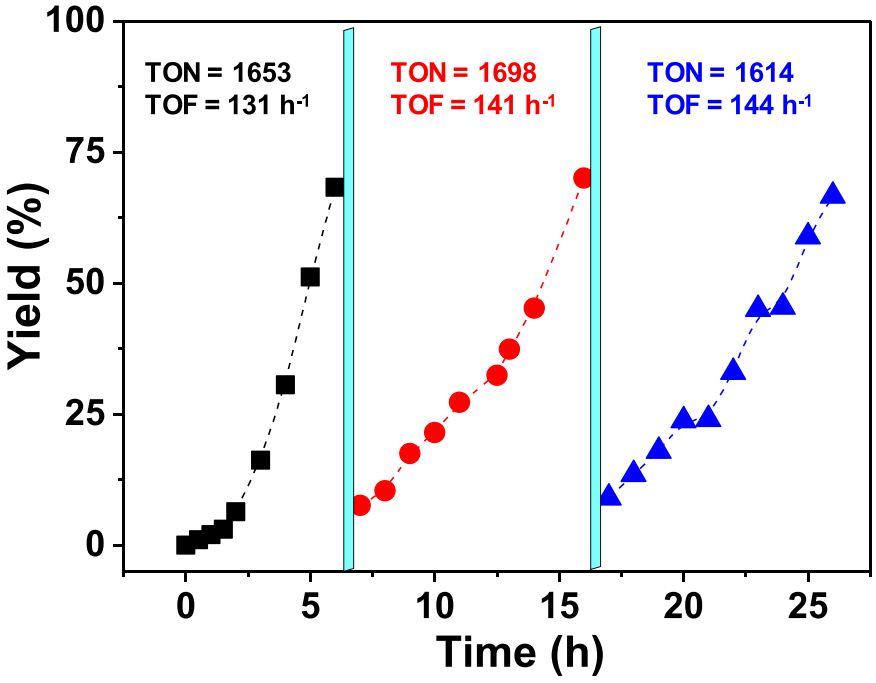

Fig. 8. 1st (black squares), 2nd (red circles) and 3th (blue triangles) reuse tests for 2 C. Broad lines in light blue indicate the injection of new batches of epichlorohydrin after each cycle. Reaction conditions: 0.5 mL epichlorohydrin, 80 °C, CO_2 balloon, solvent-free, 0.287 g of **2 C**. Yields are determined by FTIR using an appropriate calibration curve. TOF calculated after 3 h for conversion < 20%. TON at 10 h before the addition of more epichlorohydrin.

linker, or directly impregnated with $ZrCl_4$, no significant catalytic activity was observed under the same conditions (yields < 5%, entries 1–3 in Table S1). As expected, the parent **C** polymer did not promote any catalytic activity by itself. Hence, the catalytic activity of the material relied on tight cooperativity between the several sites confined in the crystalline structures grafted on the polymeric surfaces. Based on previous reports [33,34], a tentative mechanism can be proposed in which the free-carboxylate anions present in the structural defects act as co-catalyst for the epoxy-ring step of the substrate (Step 1 in Fig. 9). This pathway is likely catalyzed by the activation of the oxirane ring upon coordination with the Lewis acid Zr sites (**RIC** in Fig. 9). In a similar manner, the alkoxylate anion **Int1** formed after Step 1 can be stabilized by Zr-coordination. At this stage, the nucleophilic oxygen atom of **Int1** attacks the CO_2 molecule to produce the carboxylate anionic species **Int2**, which might also be interacting with the acidic Zr units (Step 2 in Fig. 9).

One should note that the high surface area and porosity of the MOF

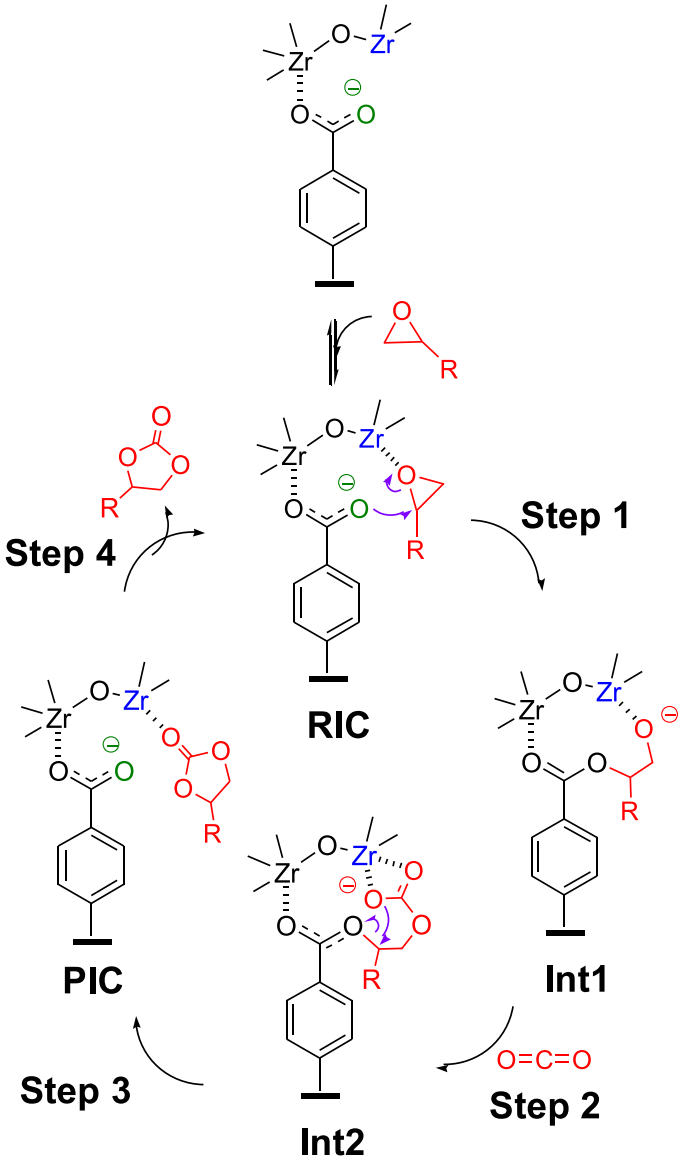

Fig. 9. Proposed mechanism for the cycloaddition of CO_2 to epichlorohydrin catalyzed by the multifunctional heterogeneous system 2 CC. Color code: red atoms correspond to reagents/products of the catalysis; Blue atoms correspond to the Lewis acid units present in the active site; Green atoms correspond to the nucleophilic species of the active site. In addition, one might note that some chloride anions present in the structure could also be acting as nucleophiles.

nanocrystals on **C** could be facilitating the adsorption of CO_2 and favoring its reaction with **Int1** [35]. **Int2** then undergoes a ring-closing step to yield the desired product that is likely stabilized by the acid sites as well (Step 3 to **PIC**, Fig. 9). Previous studies of CO_2 adsorption and desorption of similar UiO-type MOFs, have already demonstrated the presence of weak and medium to strong Lewis basic sites in bulk UiO samples [36]. They provide insights into the potential interaction of these sites with CO_2, together with the above-mentioned Lewis acid site interacting with an adsorbed epoxide. Moreover, the presence of basic oxygen sites from the organic linker coordinated with the zirconium sites of the UiO-type MOF have been modeled [37]. These sites could potentially serve as adsorption points for CO_2 during the reaction mechanism.

Finally, the cyclic carbonate is released and the carboxylate unit of the linker at the MOF defect is recovered so it can act as a nucleophile for subsequent turnovers (Step 4 in Fig. 9). It must be mentioned that some chloride anions are still present in the structure from the precursor ($ZrCl_4$) and could also be acting as the nucleophilic species for the process. However, our system does not require the use of ammonium salt additives (e.g. tetrabutylammonium bromide or TBABr) in order to achieve competitive carbonate yields with respect to state-of-art bulk carboxylate-type MOFs (mainly with UiO and MIL-type topologies) reported in the presence of TBABr as co-catalysts at room temperature conditions [38–40].

The participation of free carboxylate groups as co-catalysts (i.e. nucleophiles and/or Lewis bases) for the attack on the epoxy carbon and opening the oxirane ring (step 1) has been reported for homogeneous catalysts [41], and heterogeneous MOF catalysts [42]. In this last case, non-metal coordinated phenolate groups (i.e. at defect sites) were proposed to be the nucleophilic (and Lewis basic) oxygen atoms able to attack the CO_2, while the epoxide is simultaneously activated at the unsaturated metal sites. In a similar manner, the more defective UiO-67 should present more nucleophilic oxygen and electrophilic metal atoms as Lewis basic-acid pairs for the simultaneous activation of the CO_2 and epoxide (steps 1 and 2). In the case of the more perfect UiO-66-NH_2, the higher amount of coordinated linker-to-metal sites makes the simultaneous activation of reactants sterically unfeasible. As evidenced by the XPS analyses, we propose a mechanism for the activation of the epoxide based on the defects with acidic (Zr^{4+}) and nucleophilic (COO^-) characters present in the MOF composite. Indeed, the synergistic participation of Lewis acidic Zr^{4+} coordinatively unsaturated site and Lewis basic carboxylate ($-COO^-$) groups of non-coordinated organic linkers have been already proposed for the co-catalyst free CO_2 cycloaddition to epoxides catalyzed by zinc-carboxylate MOFs [43–45]. However, some participation of protonated carboxylic acid groups (due to the strong acid Zr sites) cannot be neglected, since the Brønsted acidity of several catalysts has been reported to promote the protonation of epoxides or their activation by hydrogen bonding [46,47].

3. Conclusions

All these results stress that the one-pot growth of model MOFs on 3D-printed polymeric supports can be achieved with a simple two-step process: (i) reaction between a nucleophile containing carboxylic groups and the epoxy-rings of the polymer followed by (ii) in-situ solvothermal formation of MOF crystal structures with the desired linkers. This synthetic protocol was found to be quite robust producing micro- and nanocrystals of UiO-66-NH_2 and UiO-67, respectively, on polymeric matrixes with varying 3D geometries (viz., A, B, and C).

The catalytic performance of these covalently-grafted MOF nanoparticles on 3D-printed polymers (i.e. 243 $mol_{product} \cdot mol_{Zr}^{-1} \cdot h^{-1}$ for sample 2 C) is superior to the state-of-art examples reported for the cycloaddition of CO_2 to epoxides with UiO-type Zr-MOFs under similar reaction conditions (19 $mol_{product} \cdot mol_{Zr}^{-1} \cdot h^{-1}$ for defect engineered bulk UiO-66-NH_2) [37]. The active sites confined within the matrix rendered a 12-fold increase in productivity in comparison with the

best-performing bulk MOF described in the literature. This, to the best of our knowledge, is the first report on co-catalyst-free CO_2 cycloaddition to epoxides using a UiO-67-based system. The best-performing material **2 C** could be recycled for at least three runs without significant loss in activity, with the active sites barely suffering from agglomeration and attrition. Preliminary tests under flow conditions infer a stable catalytic performance with a productivity value of 5.2 $mol_{product} \cdot mol_{Zr}^{-1} \cdot h^{-1}$. Thus, the proposed systems exhibit promising catalytic results under batch and flow conditions, which might pave the way to the continuous production of additional products using CO_2 as feedstock. The notable improvement observed in the catalytic performance of the MOF-3D-printed polymer hybrids not only simplifies the production of complex MOF-supported structures and enhances their recoverability but also opens up possibilities for the development of hybrid devices with superior catalytic performance in the specific transformation of interest. This advancement paves the way for the design and fabrication of more efficient and effective catalytic systems by combining the benefits of 3D printing technology with the exceptional properties of MOFs. Such hybrid devices have the potential to revolutionize various catalytic applications and contribute to the advancement of sustainable and efficient chemical processes.

Author Contributions

The manuscript was written through the contributions of all authors. All authors have given approval to the final version of the manuscript.

Supporting Information

Synthesis, characterization and catalytic tests of the MOF-polymer materials.

CRediT authorship contribution statement

Esteve Ferran: Conceptualization, Data curation, Formal analysis, Investigation, Methodology, Writing – original draft, Writing – review & editing. **Velandia Julian Sanchez:** Conceptualization, Data curation, Formal analysis, Investigation, Methodology, Validation, Visualization, Writing – original draft, Writing – review & editing. **Zanatta Marcileia:** Investigation, Writing – review & editing. **Martin Nuria:** Data curation, Formal analysis, Funding acquisition, Investigation, Writing – review & editing. **Iglesias Diego:** Investigation. **Maireles Miguel:** Data curation, Formal analysis, Investigation, Methodology. **Verdugo Eduardo García:** Conceptualization, Formal analysis, Funding acquisition, Investigation, Methodology, Project administration, Supervision, Writing – original draft, Writing – review & editing. **Cirujano Francisco G:** Conceptualization, Formal analysis, Funding acquisition, Investigation, Methodology, Supervision, Writing – original draft, Writing – review & editing. **Sans Victor:** Conceptualization, Data curation, Funding acquisition, Investigation, Writing – review & editing.

Declaration of Competing Interest

The authors declare that they have no known competing financial interests or personal relationships that could have appeared to influence the work reported in this paper.

Data availability

No data was used for the research described in the article.

Acknowledgments

J. S. V. acknowledges Universidad Jaume I (Pla dePromocio de la Investigacio de la Universitat Jaume I) for a Post-Doctoral Fellowship. Universidad Jaume I is also acknowledged for the UJI-B2021–31 project. F. G: C. and N. M. acknowledge the “Ramon y Cajal” contract with code RYC2020–028681-I and RYC2021–033167-I funded MCIN/AEI/10.13039/501100011033 and by "ESF investing in your future", “European Union NextGenerationEU/PRTR”. The Spanish Ministry of Science is also acknowledged for the PID2022–142897OA-I00, PID2021–124695OB-C-22, TED2021–129626B-C22 and TED2021–130288B-I00 projects funded by MCIN/AEI/10.13039/501100011033 and by the “European Union” or by the “European Union NextGenerationEU/PRTR”. VS and FGC thank Generalitat Valenciana (CIDEGENT 2018/036 and CISEJI/2023/78, respectively) for funding. MZ acknowledges funding from EU through the MSCA program (GA 101026335).

Appendix A. Supporting information

Supplementary data associated with this article can be found in the online version at doi:10.1016/j.jcou.2023.102636.

References

[1] O.M. Yaghi, H.C. Zhou, J.R. Long, Introduction to metal – organic frameworks, Chem. Rev. 112 (2012) 673–674.
[2] A. Bavykina, N. Kolobov, S. Khan, J.A. Bau, A. Ramirez, J. Gascon, Metal–organic frameworks in heterogeneous catalysis: recent progress, new trends, and future perspectives, Chem. Rev. 120 (16) (2020) 8468–8535.
[3] D. Yang, B.C. Gates, Catalysis by metal organic frameworks: perspective and suggestions for future research, ACS Catal. 9 (3) (2019) 1779–1798.
[4] V. Pascanu, G. González Miera, A.K. Inge, B. Martín-Matute, Metal–organic frameworks as catalysts for organic synthesis: a critical perspective, J. Am. Chem. Soc. 141 (18) (2019) 7223–7234.
[5] Q. Wang, D. Astruc, State of the art and prospects in metal–organic framework (MOF)-based and MOF-derived nanocatalysis, Chem. Rev. 120 (2) (2020) 1438–1511.
[6] Z. Wang, L. Liu, Z. Li, N. Goyal, T. Du, J. He, G.K. Li, Shaping of metal–organic frameworks: a review, Energy Fuels 36 (6) (2022) 2927–2944.
[7] Y. Li, G. Wen, J. Li, Q. Li, H. Zhang, B. Tao, J. Zhang, Synthesis and shaping of metal–organic frameworks: a review, Chem. Commun. 58 (2022) 11488–11506.
[8] P. Falcaro, R. Ricco, C.M. Doherty, K. Liang, A.J. Hill, M.J. Styles, MOF positioning technology and device fabrication, Chem. Soc. Rev. 43 (2014) 5513–5560.
[9] O. Halevi, J.M.R. Tan, P.S. Lee, S. Magdassi, Hydrolytically stable MOF in 3D-printed structures, Adv. Sustain. Syst. 2 (2018) 2–6.
[10] S. Lawson, M. Snarzyk, D. Hanify, A.A. Rownaghi, F. Rezaei, Development of 3D-printed polymer-MOF monoliths for CO_2 adsorption, Ind. Eng. Chem. Res. 59 (15) (2020) 7151–7160.
[11] I. Pellejero, F. Almazán, M. Lafuente, M.A. Urbiztondo, M. Drobek, M. Bechelany, A. Julbe, L.M. Gandía, Functionalization of 3D printed ABS filters with MOF for toxic gas removal, J. Ind. Eng. Chem. 89 (2020) 194–203.
[12] A. Figuerola, D.A.V. Medina, A.J. Santos-Neto, C. Palomino Cabello, V. Cerdà, G. Turnes Palomino, F. Maya, Metal–organic framework mixed-matrix coatings on 3D printed devices, Appl. Mater. Today 16 (2019) 21–27.
[13] W. Liu, O. Erol, D.H. Gracias, 3D printing of an in situ grown MOF hydrogel with tunable mechanical properties, ACS Appl. Mater. Interfaces 12 (29) (2020) 33267–33275.
[14] S. Waheed, M. Rodas, H. Kaur, N.L. Kilah, B. Paull, F. Maya, In-situ growth of metal-organic frameworks in a reactive 3D printable material, Appl. Mater. Today 22 (2021), 100930.
[15] M. Ramezanzadeh, B. Ramezanzadeh, G. Bahlakeh, A. Tati, M. Mahdavian, Development of an active/barrier bi-functional anti-corrosion system based on the epoxy nanocomposite loaded with highly-coordinated functionalized zirconium-based nanoporous metal-organic framework (Zr-MOF), Chem. Eng. J. 408 (2021), 127361.
[16] C. Hu, J.D. Xiao, X.D. Mao, L.L. Song, X.Y. Yang, S.J. Liu, Toughening mechanisms of epoxy resin using aminated metal-organic framework as additive, Mater. Lett. 240 (2019) 113–116.
[17] F. Seidi, M. Jouyandeh, M. Taghizadeh, A. Taghizadeh, H. Vahabi, S. Habibzadeh, K. Formela, M.R. Saeb, Metal-organic framework (MOF)/epoxy coatings: a review, Materials 13 (2020).
[18] M. Fiaz, J. Lin, S. He, Synthesis and dielectric behavior of zirconium-based metal-organic framework UiO-66 filled epoxy composites, Mater. Today Proc. 47 (2020) S121–S124.
[19] D. Valverde, R. Porcar, M. Zanatta, S. Alcalde, B. Altava, V. Sans, E. García-Verdugo, Towards highly efficient continuous-flow catalytic carbon dioxide cycloadditions with additively manufactured reactors, Green Chem. (2022) 3300–3308.
[20] H. Molavi, A. Eskandari, A. Shojaei, S.A. Mousavi, Enhancing CO_2/N2 adsorption selectivity via post-synthetic modification of NH2-UiO-66(Zr), Microporous Mesoporous Mater. 257 (2018) 193–201.
[21] Jared B. DeCoste, Gregory W. Peterson, Himanshu Jasuja, T.Grant Glover, Yougui Huang, Krista S. Walton, Stability and degradation mechanisms of metal–organic frameworks containing the Zr6O4(OH)4 secondary building unit, J. Mater. Chem. A 1 (2013) 5642–5650.

[22] J. Sunil, C. Narayana, G. Kumari, K. Jayaramulu, Raman spectroscopy, an ideal tool for studying the physical properties and applications of metal–organic frameworks (MOFs), Chem. Soc. Rev. 52 (2023) 3397–3437.
[23] M. Sen Bishwas, M. Malik, P. Poddar, Raman spectroscopy-based sensitive, fast and reversible vapour phase detection of explosives adsorbed on metal–organic frameworks UiO-67, N. J. Chem. 45 (2021) 7145–7153.
[24] Li, L. Wang, P. Dai, L. Yan, L. Cao, X. Gu, X. Zhao, Missing-node directed synthesis of hierarchical pores on a zirconium metal–organic framework with tunable porosity and enhanced surface acidity via a microdroplet flow reaction, J. Mater. Chem. A 5 (2017) 22372–22379.
[25] S. Mukhopadhyay, R. Shimoni, I. Liberman, R. Ifraemov, I. Rozenberg, I. Hod, Assembly of a metal–organic framework (MOF) membrane on a solid electrocatalyst: introducing molecular-level control over heterogeneous CO_2 reduction, Angew. Chem. 133 (2021) 13535–13541.
[26] J. Shankwitz, D. Speed, D. Sinanan, G. Szulczewski, The effects of functional groups and missing linkers on the adsorption capacity of aromatic hydrocarbons in uio-66 thin films, Inorganics 9 (2021) 1, https://doi.org/10.3390/inorganics9010001.
[27] B.T. Yost, B. Gibbons, A. Wilson, A.J. Morris, L.E. McNeil, Vibrational spectroscopy investigation of defects in Zr- and Hf-UiO-66, RSC Adv. 12 (2022) 22440–22447.
[28] H. Büttner, L. Longwitz, J. Steinbauer, C. Wulf, T. Werner, Recent developments in the synthesis of cyclic carbonates from epoxides and CO_2, Top. Curr. Chem. 375 (2017) 50.
[29] M. Alves, B. Grignard, R. Mereau, C. Jerome, T. Tassaing, C. Detrembleur, Organocatalyzed coupling of carbon dioxide with epoxides for the synthesis of cyclic carbonates: catalyst design and mechanistic studies, Catal. Sci. Technol. 13 (2017) 2651–2684.
[30] A.J. Kamphuis, F. Picchionia, P.P. Pescarmona, CO_2-fixation into cyclic and polymeric carbonates: principles and applications, Green Chem. 21 (2019) 406–448.
[31] G. Fu, F.G. Cirujano, A. Krajnc, G. Mali, M. Henrion, S. Smolders, D.E. De Vos, Unexpected linker-dependent Brønsted acidity in the (Zr)UiO-66 metal organic framework and application to biomass valorization, Catal. Sci. Technol. 10 (2020) 4002–4009.
[32] F.G. Cirujano, F.X. Llabrés i Xamena, Tuning the catalytic properties of UiO-66 metal–organic frameworks: from lewis to defect-induced Brønsted acidity, J. Phys. Chem. Lett. 11 (2020) 4879–4890.
[33] Z. Zhao, J. Qin, C. Zhang, Y. Wang, D. Yuan, Y. Yao, Recyclable single-component rare-earth metal catalysts for cycloaddition of CO_2 and epoxides at atmospheric pressure, Inorg. Chem. 56 (2017) 4568–4575.
[34] M. North, R. Pasquale, Mechanism of cyclic carbonate synthesis from epoxides and CO_2, Angew. Chem., Int. Ed. 48 (2009) 2946–2948.
[35] W. Clegg, R.W. Harrington, M. North, R. Pasquale, Cyclic carbonate synthesis catalysed by bimetallic aluminium–salen complexes, Chem. – Eur. J. 16 (2010) 6828–6843.
[36] J. Kim, S.N. Kim, H.G. Jang, G. Seo, W.S. Ahn, CO_2 cycloaddition of styrene oxide over MOF catalysts, Appl. Catal. A 453 (2013) 175–180.
[37] C. Caratelli, J. Hajek, F.G. Cirujano, M. Waroquier, F.X. Llabrés i Xamena, V. Van Speybroeck, Nature of active sites on UiO-66 and beneficial influence of water in the catalysis of Fischer esterification, J. Catal. 352 (2017) 401–414.
[38] S. Payra, S. Roy, CO_2 cycloaddition reaction at ambient temperature and pressure over metal organic framework catalysts, MRS Commun. 13 (2023) 1309–1314.
[39] S. Payra, Roy, From trash to treasure: probing cycloaddition and photocatalytic reduction of CO_2 over cerium-based metal−organic frameworks, J. Phys. Chem. C 125 (2021) 8497–8507.
[40] T.K. Pal, D. De, P.K. Bharadwaj, Metal–organic frameworks for the chemical fixation of CO_2 into cyclic carbonates, Coord. Chem. Rev. 408 (2020), 213173.
[41] N. Liu, Y.F. Xie, C. Wang, S.J. Li, D. Wei, M. Li, B. Dai, Cooperative multifunctional organocatalysts for ambient conversion of carbon dioxide into cyclic carbonates, ACS Catal. 8 (2018) 9945–9957.
[42] K. Xu, A.M.P. Moeljadi, B.K. Mai, H. Hirao, How does CO_2 react with styrene oxide in Co-MOF-74 and Mg-MOF-74? catalytic mechanisms proposed by QM/MM calculations, J. Phys. Chem. C 122 (1) (2018) 503–514.
[43] S. Singh Dhankhar, B. Ugale, C.M. Nagaraja, Co-catalyst-free chemical fixation of CO_2 into cyclic carbonates by using metal-organic frameworks as efficient heterogeneous catalysts, Chem. Eur. J. 15 (2020) 2403–2427.
[44] X. Huang, Y. Chen, X. Lin, X. Ren, Y. Song, Z. Xu, X. Dong, X. Li, C. Hu, B. Wang, Zn-BTC MOFs with active metal sites synthesized via a structure-directing approach for highly efficient carbon conversion, Chem. Commun. 50 (2014) 2624–2627.
[45] X. Liu, C. Hu, J. Wu, P. Cui, F. Wei, Defective NH2-UiO-66 (Zr) effectively converting CO_2 into cyclic carbonate under ambient pressure, solvent-free and co-catalyst-free conditions, Chin. J. Chem. Eng. 43 (2022) 222–229.
[46] B. Li, L. Zhang, Y. Song, D. Bai, H. Jing, Brønsted acid improved cycloaddition of carbon dioxide to propylene oxide, J. Mol. Catal. 363–364 (2012) 26–30.
[47] L.-F. Xiao, D.-W. Lv, D. Su, W. Wu, H.-F. Li, Influence of acidic strength on the catalytic activity of Brønsted acidic ionic liquids on synthesizing cyclic carbonate from carbon dioxide and epoxide, J. Clean. Prod. 67 (2014) 285–290.